RCS-Based 3D Millimeter-Wave Channel Modeling Using Quasi-Deterministic Ray Tracing

Ebrahimizadeh, Javad; Madannejad, Alireza; Cai, Xuesong; Vinogradov, Evgenii; Vandenbosch, Guy A.E.

Published in:
IEEE Transactions on Antennas and Propagation

DOI:
10.1109/TAP.2024.3365859

2024

RCS-Based 3D Millimeter-Wave Channel Modeling Using Quasi-Deterministic Ray Tracing

Javad Ebrahimizadeh, Alireza Madannejad, Xuesong Cai, *Senior Member, IEEE,* Evgenii Vinogradov, and Guy A. E. Vandenbosch, *Fellow, IEEE*

***Abstract*—This paper introduces a low-complexity ultra-wideband quasi-deterministic ray tracing (QD-RT) method for statistical analysis of wireless channels. This model uses a statistical distribution to model the bistatic radar-cross-section (RCS) of irregular objects such as cars and pedestrians, instead of a deterministic propagation model, i.e., applying the exact values of bistatic RCSs. It is shown that the quasi-deterministic propagation model benefits from a low complexity compared with a deterministic model while keeping the accuracy. The proposed QD-RT method is applied in a realistic street canyon scenario in the millimeter wave frequency band, and the performance of the QD-RT method is verified by the deterministic propagation method, where the second-order statistics including root-mean-square (RMS) delay spread and angular spread and the first-order statistic transfer function yield good agreements. Finally, the application of the QD-RT in stochastic channel modeling is demonstrated by developing a 3GPP-like statistical channel model for street canyon scenarios.**

***Index Terms*—Ray tracing; street canyon; radar cross section; channel model; mmWave propagation, transfer function; path loss; RMS delay spread; power delay profile; probability density function.**

I. Introduction

MILLIMETER-wave (mmWave) communication in dense urban micro-cellular outdoor scenarios such as street canyons, offers the advantages of high data rates and low latency [1]–[3]. However, at these frequencies, path loss is a significant issue that must be addressed. This can be mitigated through the use of massive multiple-input multiple-output (MIMO) techniques, beamforming, and deploying a network of small cell base stations [4]–[8].

Optimizing the performance of mmWave communication systems in a street canyon scenario requires a thorough understanding of the mmWave propagation characteristics. Although measurement campaigns can be alternatives, they are limited and costly. Therefore, numerical methods such as ray tracing are essential for accurately modeling the channel [8]–[10]. Accurately calculating wave propagation in street canyon scenarios with the presence of complex and electrically large (compared to wavelength) irregular objects such as cars, pedestrians, traffic signs, and lampposts is a challenging task. This task is particularly demanding to balance computational speed and simulator accuracy.

The MiWEBA and NIST projects proposed a quasi-deterministic ray tracing method that generates power and delays deterministically from scenario-defined macro objects such as walls and grounds, while parameters of rays due to random, irregular objects are selected from predefined distributions [11]–[17]. However, the proposed method is not based on the bistatic radar-cross-section (RCS) of the object, which decreases the accuracy of the method.

The bistatic radar cross-section (RCS) of well-defined shapes, such as lampposts and traffic signs, can be determined analytically. In [18], [19], the authors used an analytical RCS model of traffic signs at 5.9 GHz and integrated them into a ray tracing technique to develop a vehicle-to-everything communication channel model. In [20], the authors implemented the analytical bistatic RCS of the lamppost in a 3D ray tracing tool to enhance the propagation model's accuracy and realism. They showed that lampposts significantly contribute to the large-scale propagation model.

Irregular objects can be simplified with well-defined shapes, such as a sphere or a rectangular surface. The METIS channel model uses the RCS model of a sphere for scattering from irregular objects [21]. However, this approach has limitations in modeling the bistatic RCS of irregular objects. The RCS of an electrically large sphere is constant and not a function of spatial angles, which results in a failure to accurately capture the fluctuation of bistatic RCS. Furthermore, METIS determines the sphere's radius to match the surface area covering the physical size of the irregular object, and its electrical size is not considered. The analytical mmWave scattering model based on the 3D Fresnel model for rectangular surfaces, described in [22]–[24], was developed for modeling the bistatic RCS of irregular objects with a well-defined rectangular plate shape.

The bistatic RCS of irregular objects can be computed using asymptotic methods, such as physical optics (PO) and geometrical optics (GO) methods. In [25], the authors proposed a simplified ray tracing method based on the scattering center method. By estimating the dominant current distributions on the surface of irregular objects, this method

This work was supported in part by the European Union's Framework Programme for Research and Innovation Horizon 2020 under the Marie Skłodowska-Curie Grant Agreement No. 861222 (MINTS project), the Horizon Europe Framework Programme under the Marie Skłodowska-Curie grant agreement No. 101059091, the Swedish Research Council (Grant No. 2022-04691), the strategic research area ELLIIT, Excellence Center at Linköping — Lund in Information Technology, and the Crafoord Foundation.

Guy A. E. Vandenbosch, Evgenii Vinogradov, and Javad Ebrahimizadeh are with the Department of Electrical Engineering, Division ESAT-WaveCoRE, Katholieke Universiteit Leuven, B-3001, Leuven, Belgium e-mail: (guy.vandenbosch@esat.kuleuven.be).

Alireza Madannejad is with the Division of Micro- and Nanosystems, KTH Royal Institute of Technology, 100 44 Stockholm, Sweden.

Xuesong Cai is with the Department of Electrical and Information Technology, Lund University, 22363 Lund, Sweden.

Evgenii Vinogradov is with Technology Innovation Institute, UAE.

can compute far-field and near-field RCS values. Nonetheless, it is more complex than the traditional physical optics method.

Treating the RCS as a random variable in the frequency and spatial domain with a particular distribution can model the fluctuations. This approach is commonly used in radar and wireless communication applications, where RCS fluctuations are modeled based on specific power density functions (PDFs) [26]–[28]. In [29], the authors demonstrated that the bistatic RCS of complex objects can be modeled using a statistical distribution. They also modeled several types of vehicles, such as passenger cars, vans, and trucks, with logistic distributions in the sub-6 GHz band. However, their work focused on classification rather than incorporating the RCS distribution into a realistic channel propagation model.

To the authors' knowledge, for the first time, the present paper introduces a new method for ray tracing, i.e., quasi-deterministic ray tracing (QD-RT), which incorporates the statistical distributions of the bistatic RCSs of irregular objects instead of their exact values. The QD-RT method is suitable for statistical analysis of channels. The development of the QD-RT method is motivated by the need for an accurate simulation of statistical channels in real-life scenarios, such as street canyons. It is shown that the proposed method can generate the same channel parameter distributions as the deterministic ray tracing. This paper employs the QD-RT method to develop a 3GPP-like statistical channel model for the street canyon scenario. In this scenario, transmitter antennas are mounted on lampposts in the street, providing service to sidewalk users. The main contributions of the paper are:

- **Quasi-deterministic Ray Tracing Technique:** A novel quasi-deterministic ray tracing technique is developed utilizing dedicated PDFs of bistatic RCSs of objects. This technique enables accurate modeling of the complex propagation environment, allowing for a realistic assessment of the wireless communication channels. The quasi-deterministic ray tracing benefits from low computational complexity and can generate the same channel distributions as the deterministic ray tracing method.
- **Probabilistic Angular Modeling of Bistatic RCS:** A dedicated procedure for statistical modeling of bistatic RCS is proposed where the spatial angular dependency is explicitly considered in the modeling process. The proposed model effectively represents the angular functionality of bistatic RCS through statistical modeling. The angular functionality of the statistical RCS (the PDF of bistatic RCS) is modeled with a probability density function denoted by $f_{\Theta,\Phi}(\theta,\phi)$, where θ and ϕ are spatial angles in spherical coordinates. This function represents the likelihood of an irregular object being illuminated by the transmitter antenna at the incident angle and observed by the receiver at the reflected angle. The associated angular PDF at the spatial angles θ and ϕ is determined by the ratio of the differential area that an omnidirectional antenna illuminates to the total possible area it can illuminate.
- **Efficient Calculation of Bistatic RCSs:** Using the PO-Gordon technique to calculate the bistatic RCSs of complex objects brings efficiency and accuracy to the modeling process. This enables faster computation of the RCS values, which is used to derive statistical RCS with low complexity. In addition, it is needed in the deterministic ray tracing method due to its low complexity and high accuracy.
- **Development of a Dedicated Procedure:** The paper articulates a dedicated 3GPP-like procedure for reproducing statistical channel coefficients. This procedure outlines the steps required to generate the statistical channel coefficients. Additionally, the paper proposes a statistical model tailored for the street canyon scenario, incorporating close-in path loss based on statistical bistatic RCS.

The rest of the paper is organized as follows. Section II describes the theory of quasi-deterministic ray tracing and illustrates the specific topology of the street canyon scenario. Section III validates the quasi-deterministic propagation technique and shows that it can generate the same channel parameter distributions as the deterministic ray tracing (D-RT) method. Section IV provides the geometry-based stochastic radio channel model and illustrates a 3GPP-like approach for model implementation. Finally, the paper is concluded in Section V. In this paper, the letter x represents a scalar, the letter with an arrow $\vec{x}$ represents a vector, and the letter with a hat $\hat{x}$ represents a unit vector.

II. METHOD

In this section, we present a comprehensive overview of the street canyon topology, which is a common dense scenario in wireless channel modeling. We first review the theory of wave propagation using ray tracing techniques. We then introduce a novel quasi-deterministic ray tracing method to statistically characterize the channel. This method allows for a detailed analysis of the propagation phenomena, which is essential for the design and optimization of wireless communication systems in complex urban environments.

A. Street canyon scenario topology

As shown in Fig. 1, the street canyon scenario consists of tall buildings on both sides of a street and objects such as lampposts, parked cars, and pedestrians placed. The street length and width are denoted as W_1 and L_1, and the sidewalk width is indicated by W_2. The walls with the thickness of D_{w} are assumed to be made of bricks with a relative permittivity of $\epsilon_{\mathrm{r,w}}$ at operational frequency f_0. The ground is assumed to be dry ground with a relative permittivity of $\epsilon_{\mathrm{r,g}}$. The transmitter (TX) and receiver (RX) antennas are omnidirectional antennas with vertical polarization. The location of the transmitter and receiver are denoted by $(X_{\mathrm{tx}}, Y_{\mathrm{tx}}, Z_{\mathrm{tx}})$ and $(X_{\mathrm{rx}}, Y_{\mathrm{rx}}, Z_{\mathrm{rx}})$, respectively. The pedestrians are on the sidewalks, and the cars are parked along the street. The wall at the TX side is located at the plane $y = Y_{\mathrm{w1}}$, and the RX side is located at the plane $y = Y_{\mathrm{w2}}$. An overview of the simulation scenario is given in Table I.

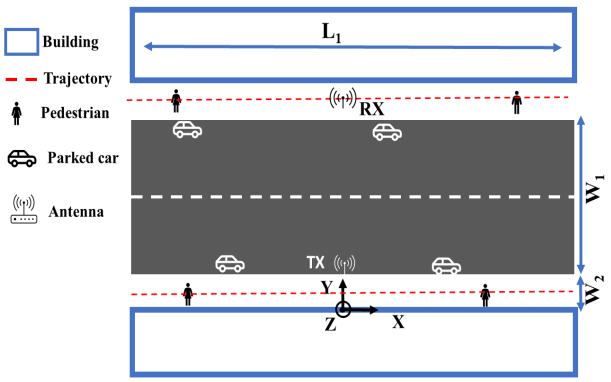

(a) Top view of the Street Canyon scenario.

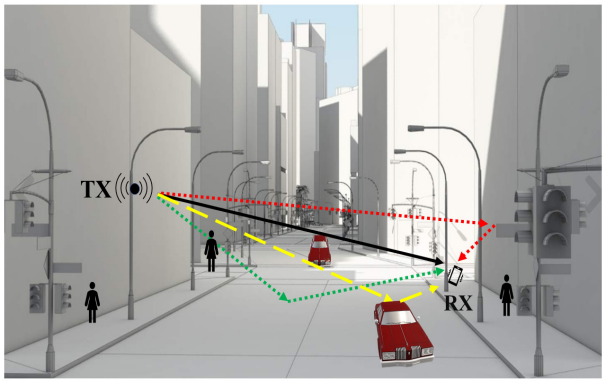

(b) Perspective view of Street Canyon scenario. The solid line is LOS, dotted lines are reflected rays, and the dashed line shows scattered rays.

Fig. 1: Street canyon scenario topology consisting of line-of-sight, reflected, scattered paths [30].

TABLE I: Overview of simulation scenario.

Object	Parameters	Simulation values
Frequency range	Bandwidth	59-61 GHz
Antenna	Type	Omnidirectional
	$(X_{\text{tx}}, Y_{\text{tx}}, Z_{\text{tx}})$	$(0, 2, 3.5)$[m]
	Y_{rx}^{*}	1 or 15 [m]
	Z_{rx}	1 [m]
	Polarization	V-V
Pedestrian	Length : L_{p}	0.4 [m]
	Width : W_{p}	0.4 [m]
	Height : H_{p}	1.8 [m]
	Minimum separation distance	1 [m]
	Movement speed	0 [m/s]
Parked car	Length : L_{c}	4.55 [m]
	Width : W_{c}	1.77 [m]
	Height : H_{c}	1.24 [m]
	Minimum separation distance	2.5 [m]
	Movement speed	0 [m/s]
Sidewalk	Length : L_1	150 [m]
	Width : W_2	2 [m]
Street	Length : L_1	150 [m]
	Width : W_1	12 [m]
Wall	Length : L_{w}	150 [m]
	Thickness : D_{w}	10 [cm]
	Height: H_{w}	Infinite
	Relative permittivity**: $\epsilon_{\text{r,w}}$	3.26
	locations: Y_{w1} and Y_{w2}	(0 and 16) [m]
Ground	Type	Dry ground
	Relative permittivity ** : $\epsilon_{\text{r,g}}$	6

*The RX follows the trajectory path illustrated by red-dash line in Fig. 1(a).
**The relative permittivity is provided in [31], [32] .

B. Deterministic Ray Tracing method

This subsection describes the theoretical deterministic channel model specifically developed for the street canyon scenario. The signal model for a channel that consists of M ray paths is denoted as:

$$H(f) = \sum_{i=0}^{M-1} \alpha_i(f) e^{-j2\pi f \tau_i} a_{\text{R}}(\Theta_{\text{AoA},i}, f) a_{\text{T}}(\Theta_{\text{AoD},i}, f), \quad (1)$$

where α_i and τ_i represent the path amplitude and propagation delay for the i^{th} path, respectively. The antenna patterns (that can be frequency dependent) of the transmitter and the receiver are $a_{\text{T}}(\Theta_{\text{AoD},i}, f)$ and $a_{\text{R}}(\Theta_{\text{AoA},i}, f)$ at the angle of departure $\Theta_{\text{AoD},i}$ and the angle of arrival $\Theta_{\text{AoA},i}$, respectively. By further distinguishing the Line of Sight (LOS), reflected, and scattered components, we have

$$H(f) = H_0(f) + \sum_{m=1}^{M_{\text{r}}} H_m^{\text{r}}(f) + \sum_{n=1}^{N_{\text{s}}} H_n^{\text{s}}(f), \quad (2)$$

$$H_0(f) = \alpha_0(f) e^{-j2\pi f \tau_0} a_{\text{R}}(\Theta_{\text{AoA},0}, f) a_{\text{T}}(\Theta_{\text{AoD},0}, f), \quad (3)$$

$$H_m^{\text{r}}(f) = \alpha_m^{\text{r}}(f) e^{-j(2\pi f \tau_m^{\text{r}} + \phi^{\text{r}})} a_{\text{R}}(\Theta_{\text{AoA},m}, f) a_{\text{T}}(\Theta_{\text{AoD},m}, f), \quad (4)$$

$$H_n^{\text{s}}(f) = \alpha_n^{\text{s}}(f) e^{-j(2\pi f \tau_n^{\text{s}} + \phi^{\text{s}})} a_{\text{R}}(\Theta_{\text{AoA},n}, f) a_{\text{T}}(\Theta_{\text{AoD},n}, f), \quad (5)$$

where $H_0(f)$ is the LOS contribution, and $H_m^{\text{r}}(f)$ and $H_n^{s}(f)$ are the transfer functions due to the m^{th} reflections from walls and the transfer function due to the n^{th} point scatterers, namely pedestrians and parked cars, respectively. The total number of reflectors and scatterers are M_{r} and N_{s}, respectively. The channel coefficient for the LOS, reflection, and scattered rays are denoted by α_0, α_m^{r}, and α_n^{s}, respectively. They are denoted as:

$$|\, \alpha_0(f) \,|^2 = \left(\frac{c_0}{4\pi f r_0}\right)^2, \quad (6)$$

$$|\, \alpha_m^{\text{r}}(f) \,|^2 = \left(\frac{c_0 R^{\text{TE/TM}}}{4\pi f (r_1 + r_2)}\right)^2, \quad (7)$$

$$|\, \alpha_n^{\text{s}}(f) \,|^2 = \frac{1}{4\pi r_1^2} \times \sigma_{\text{p,q}} \times \frac{1}{4\pi r_2^2} \times \frac{c_0^2}{4\pi f^2}, \quad (8)$$

where the reflection coefficient $R^{\text{TE/TM}}$ for both TE and TM polarization is presented in [33], [34]. Also, $\sigma_{\text{p,q}}$ is the bistatic RCS of the scatterer, and the subscripts "p" or "q" represent either vertical or horizontal polarization. In this paper, the bistatic RCS values of complex objects (such as cars or pedestrians) are computed by the Physical Optics Gordon (PO-Gordon) method (see Appendix A). Additionally, r_1 is the distance between TX and the m^{th} specular point (n^{th} scatterer),

and r_2 is the distance between the m^{th} specular point (n^{th} scatterer) and the RX. The propagation delays are:

$$\tau_0 = \frac{r_0}{c_0}, \tag{9}$$

$$\tau_m^{\text{r}} \quad \text{or} \quad \tau_n^{\text{s}} = \frac{(r_1 + r_2)}{c_0}, \tag{10}$$

where c_0 is the speed of light in free space, and r_0 represents the distance between the TX and RX. For each path there are thus three channel coefficients: α^ν, τ^ν, and ϕ^ν. The coefficient α^ν represents the amplitude of the transfer function of a single reflected/scattered wave, τ^ν represents the delay time, and ϕ^ν represents the added phase due to the reflection/scattering from the object, where the superscript ν represents "r" for reflection or "s" for scattering, respectively. In this paper, the corresponding path loss in dB is:

$$PL = -20 \log_{10}(|\alpha^\nu|). \tag{11}$$

It is important to note that in a ray tracing model, the calculation of AoA and AoD is inherently connected to the geometric features of the environment and the reflections or diffractions that occur. While explicit antenna patterns may not be included in the channel model, the angles are determined based on the interactions of the waves with the surrounding objects.

C. Quasi-Deterministic Ray Tracing method

The quasi-deterministic ray tracing method employs the PDF of bistatic RCS instead of its exact value to reduce computational complexity significantly. This method provides a low-complexity approach for statistically analyzing and modeling the channel, which requires Monte Carlo simulations. In such simulations, certain variables need to be randomly varied during each iteration. For instance, to statistically analyze the path loss due to irregular objects using (8), the distance between the object and the transmitter and receiver antennas, represented by r_1 and r_2 respectively, are considered independent continuous random variables X_1 and X_2. Therefore, using (11), the path loss can be represented as a random variable denoted by:

$$\begin{aligned} PL(X_1, X_2) \sim & -10 \log_{10}\left(\frac{\lambda^2}{(4\pi)^3}\right) + \\ & 20 \log_{10}(X_1) + 20 \log_{10}(X_2) - 10 \log_{10}(\sigma_{\text{pq}}). \end{aligned} \tag{12}$$

According to (12), using the PDF of the bistatic RCS of objects can generate the same distribution for the path loss as using the exact values of bistatic RCS.

The goal is to determine the PDF of the RCS for irregular objects. This is achieved by calculating the bistatic RCS for all incident and scattered angles, which requires generating a dataset. However, it is important to note that the contribution of spatial angles to the bistatic RCS dataset is not equal and depends on the specific scenario being tested. In the case of a street canyon scenario, the angular dependency of the bistatic RCS can be modeled by the probability density function of area coverage in spherical coordinates. Once the dataset is generated, an appropriate PDF can be assigned to it. In the following subsections, the angular dependency and generating the corresponding PDF for bistatic RCS are explained in detail.

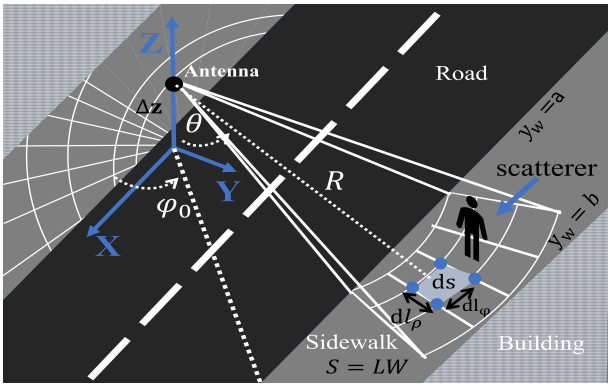

Fig. 2: Area coverage for different incident/scattered elevation angles.

1) Angular dependence: In the street canyon scenario, the probability of having a specific incident/scattered angle combination is not uniform. The reason is the fact that for a specific elevation angle interval $\Delta\theta$ and azimuth angle interval $\Delta\phi$, the illumination area on the ground in the scenario differs for different θ and ϕ, as shown in Fig. 2. For example, it is easily seen that the coverage area on the ground increases with increasing elevation angles. To derive the angular dependency, we can utilize Fig. 2, which represents an omnidirectional antenna at a differential height of Δz illuminating the area. The probability is then associated with the portion of the area that is illuminated by the differential spatial angle. The scatterer is assumed to be located in the differential section denoted by ds in Fig. 2. In other words, the relation between these angles and the corresponding ground area determines the angular probability (the probability of obtaining a certain θ and ϕ) for a certain area probability (the probability of being in a certain ground area). In this work, it is assumed that pedestrians and parked cars are uniformly distributed over the sidewalks and beside the sidewalks, respectively. In other words, it is assumed that the probability density function in the cartesian coordinate is uniform as $f_{X,Y}(x, y) = \frac{1}{2L_1W_2}$. It is straightforward to show that for a uniform rectangle ground area with dimensions L_1 and W_2, the probability density function $f_{\Theta,\Phi}(\theta, \phi)$ for the scatterer to be located in a direction (θ and ϕ) is

$$f_{\Theta,\Phi}(\theta, \phi) = \begin{cases} \frac{(\Delta z)^2 \sin(\theta)}{2L_1W_2 \cos^3(\theta)} & \begin{cases} \frac{a}{\Delta z \times \sin(\phi)} < \tan(\theta) < \frac{b}{\Delta z \times \sin(\phi)} \\ \phi_0 < \phi < \pi - \phi_0, \end{cases} \\ 0 & \text{otherwise} \end{cases} \tag{13}$$

provided that the direction (θ and ϕ) points towards the rectangle. Here, Δz is the differential height between the antenna and the receiver. Here, the elevation angle is limited by the lines $Y_{\text{w}} = a$ and $Y_{\text{w}} = b$ and the azimuth angle is bounded by $\phi_0 = \frac{2a}{L_1}$, as shown in Fig. 2.

This expression is the basis for calculating the angular probabilities, i.e., the probability that the signal from the transmitter is reaching the scatterer from a certain incident direction and the probability that the signal has to be scattered in a certain scattering direction to reach the receiver. It is important to point out that by modeling the objects as point scatterers with a certain RCS, the phase delay due to the scattering itself is zero. The same procedure is valid for the parked car by considering the region dedicated to the parked cars.

2) Bistatic RCS distribution: The PDF of the bistatic RCS of an object can now be calculated in the following way. First, the dataset of RCSs for all combinations of incident and scattering angles is calculated. Second, the probability that a specific set of angles is occurring in the considered scenario is taken into account. As said, this probability can be derived from (13). The result is a PDF of the bistatic RCS for this specific scenario, i.e., including the probabilities linked with the rectangular area where the object may be located. This scenario-specific PDF is used in the channel model by picking a random value for an RCS value from this PDF (instead of the deterministic RCS), which takes into account the angular probabilities. Concerning frequency dependency, we can simplify the integration from Appendix (A.3) by approximating it with a linear function proportional to k_o, which represents the free space wave number. In addition, the probability of the contribution at each frequency is assumed to follow a uniform distribution.

To summarize the process of generating the final RCS's PDF, the procedure is as follows:

Step 1: Calculate the bistatic RCS for all incident and reflected angles using the Physical Optics-Gordon (PO) method. In this step, the angular dependency as the geometry of the object is included.

Step 2: Step 1 is repeated for different frequencies.

Step 3: Calculate the probability of coverage based on (13), which is the probability that a signal from the transmitter is incident on the object and the probability that the reflected signal is propagating from the object toward the receiver. In other words, (13) represents the probabilistic angular modeling of bistatic RCS.

Step 4: Consider the frequency dependency by modeling it with a uniform distribution.

Step 5: Generate the final RCS's PDF by creating a histogram of the bistatic RCS, considering the contribution of each spatial angle with its corresponding probability calculated in Step 3 and taking into account the distribution at the frequency considered, as discussed in step 4.

Finally, the steps for implementing the QD-RT method for a street canyon scenario are articulated as follows.

Step 1: Define the detailed topology of the scenario under study, as for example, in Table I.

Step 2: Position the TX and RX on the scenario and use (3) to calculate the LOS channel coefficients denoted as a_0 and τ_0.

Step 3: Position the walls on the scenario and use (4) to calculate the reflection channel coefficients denoted as α^{r} and τ^{r}. The path loss and propagation delays are calculated using (7) and (10).

Step 4: Position N_{s} irregular objects such as pedestrians and cars on the scenario and use (5) to calculate the scattered channel coefficients denoted as α^{s} and τ^{s}.

Step 5: The path loss and propagation delays are calculated using (8) and (10).

Step 6: The RCS in (8) is generated using $\sigma_{pq} = 4\pi|E_s|^2$ where the amplitude of the scattered field is selected from the amplitude distribution in Table II.

Step 7: Use the produced coefficients from previous steps in formula (2) to generate the statistical channel model.

III. Numerical results

In this section, the performance of the QD-RT method is validated by statistically characterizing the street canyon scenario given in Fig. 1 with parameter values as listed in Table I. The statistical parameters of the channel, including root-mean-square (RMS) delay spread, RMS angular spread, and path loss distributions, are studied using the QD-RT method. For comparison, the D-RT method is also used, which calculates the bistatic RCS of irregular objects using exact values instead of the PDF utilized by the QD-RT method. It is important to note that during numerical simulations for channel characterization, ray tracing considers only single bouncing for scattering and reflection.

A. Distribution of bistatic RCS of car and pedestrian

This subsection aims to numerically calculate the scenario-specific PDF of the bistatic RCS of both pedestrians and cars. Initially, the bistatic RCS of each object over all the incident and reflected angles are calculated using the PO-Gordon method. Then, based on (13), the contributions of different angles for generating the scenario-specific PDF of bistatic RCS are considered.

The bistatic scattered fields of different irregular objects are calculated using the PO-Gordon method. As shown in Fig. 3, the 3D Computer-Aided Design (CAD) models of pedestrians with different postures and sizes and cars of different types are studied. The bistatic RCS over all the incident or scattered angles and the frequencies are calculated. Since the PO-Gordon technique for metallic objects is a frequency-independent method [35], [36], the frequency dependency of RCS is considered to have a uniform distribution. Furthermore, based on the (13), the contribution of elevation and azimuth angles should be considered for the corresponding angles. The Cumulative Distribution Functions (CDFs) for the elevation and azimuth angles for the two sidewalk regions are calculated and plotted in Fig. 4 and Fig. 5, respectively. The figures reveal that for the sidewalk region near the TX (RX) antenna and the sidewalk on the other side of the street, the azimuth angles near ± 90 degrees have a minimal contribution. However, elevation angles above 85 degrees have a more than 50% contribution. Finally, for each irregular object, the real and imaginary parts of the bistatic scattered fields for all angles by considering their probability of coverage are fitted with a normal distribution, and their absolute part is fitted with a Rayleigh distribution as

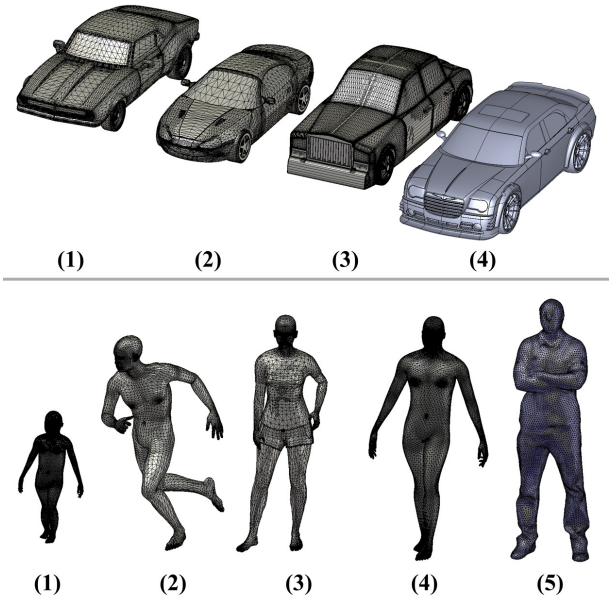

Fig. 3: Examples of the CAD models of different pedestrians and cars.

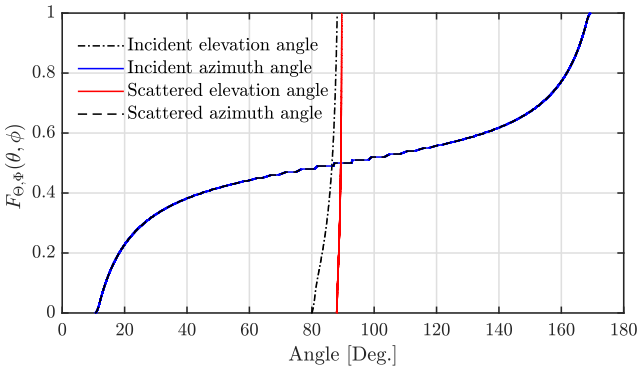

Fig. 4: CDF of elevation and azimuth angles for sidewalk far from TX(RX) antenna.

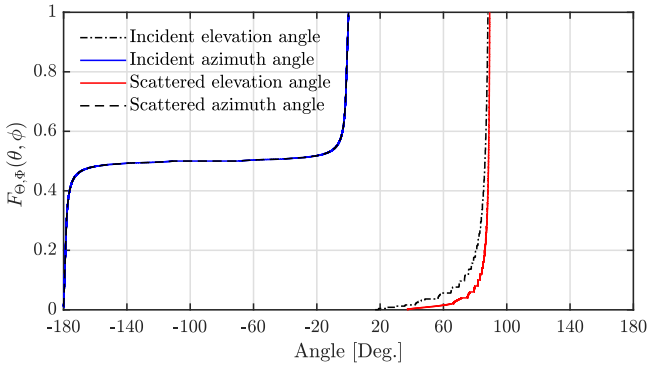

Fig. 5: CDF of elevation and azimuth angles for sidewalk near from TX (RX).

TABLE II: Statistical parameters of distributions of bistatic RCSs.

Object	Scattered electric field*			KS test** Electric field
	Real $\Re\mathfrak{e}\{s_{vv}\}$	Imaginary $\Im\mathfrak{m}\{s_{vv}\}$	Absolute $\lvert s_{vv}\rvert$	Real Imaginary Absolute
Pedestrian 1	Normal $\mu = 0.004$ $\sigma = 0.4$	Normal $\mu = 0.002$ $\sigma = 0.83$	Rayleigh scale parameter B = 0.6	Pass
Pedestrian 2	Normal $\mu = 0.1$ $\sigma = 1.35$	Normal $\mu = -0.25$ $\sigma = 0.8$	Rayleigh scale parameter B = 1.25	Pass
Pedestrian 3	Normal $\mu = 0.01$ $\sigma = 1.12$	Normal $\mu = 0.05$ $\sigma = 0.76$	Rayleigh scale parameter B = 0.96	Pass
Pedestrian 4	Normal $\mu = -0.081$ $\sigma = 0.65$	Normal $\mu = 0.015$ $\sigma = 0.93$	Rayleigh scale parameter B = 1.05	Pass
Pedestrian 5	Normal $\mu = 0.004$ $\sigma = 1.1$	Normal $\mu = 0.002$ $\sigma = 1.5$	Rayleigh scale parameter B = 1.26	Pass
Car 1	Normal $\mu = -0.74$ $\sigma = 1.23$	Normal $\mu = 0.15$ $\sigma = 1.93$	Rayleigh scale parameter B = 1.7	Pass
Car 2	Normal $\mu = -0.25$ $\sigma = 1.41$	Normal $\mu = 0.20$ $\sigma = 1.50$	Rayleigh scale parameter B = 1.45	Pass
Car 3	Normal $\mu = 0.45$ $\sigma = 2.2$	Normal $\mu = 0.17$ $\sigma = 1.65$	Rayleigh scale parameter B = 1.95	Pass
Car 4	Normal $\mu = 0.3$ $\sigma = 1.88$	Normal $\mu = .06$ $\sigma = 1.09$	Rayleigh scale parameter B = 1.53	Pass

*The bistatic RCS and the scattered electric filed follow the equation as: $\sigma_{pq} = 4\pi|s_{pq}|^2$.
**Two-sample Kolmogorov-Smirnov test

shown in TABLE II. It is observed that the amplitude of the scattered fields follows a Rayleigh distribution.

It is observed that the corresponding statistical parameters for different irregular objects vary. In simpler terms, as the irregular objects become larger, the scale parameter associated with their fitted Rayleigh distribution also increases. Furthermore, the mean and standard deviation for the normal distribution vary with different postures of pedestrians.

B. Channel characterization

The deterministic ray tracing approach serves as a benchmark model for evaluating the performance of the Quasi-Deterministic Ray Tracing (QD-RT) model. To verify the performance of the QD-RT method, three key aspects of channel characteristics, namely RMS delay spreads, RMS azimuth spreads, and the received power for a 0 dBm transmitted power, are statistically analyzed using both QD-RT and D-RT methods. Here, only the irregular objects are considered because the only difference between the QD-RT and D-RT methods is the calculation of the bistatic RCS of the irregular objects. The scenario involves the random placement of 10 pedestrians on both sidewalks and 10 cars positioned along the street. The specific details of this simulation scenario can be found in Table I. The channel parameters are recorded for different locations of RX along the trajectory path shown in Fig. 1. Totally 100 different positions are performed for RX. Moreover, to analyze the received power and RMS delay spread, we exclude LOS propagation and reflections from lampposts and walls, as their behavior is deterministic, and our focus is on scattering paths caused by irregular objects.

The RMS delay spread and angular spread are calculated using the same methodology as in [37]. It is observed that the QD-RT can generate the same distributions as the D-RT method for both the first-order statistic transfer function (received power) and the second-order statistic parameters, such as the RMS delay spread or angular spread as shown in Fig. 6, Fig. 7 and Fig. 8. The adequacy of the fitted

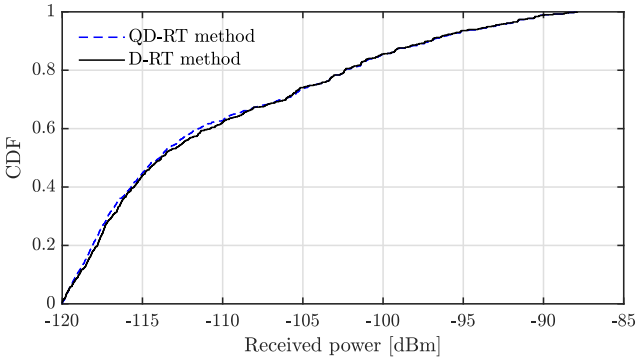

Fig. 6: CDF of received power for the RX located along the trajectory path on the sidewalk.

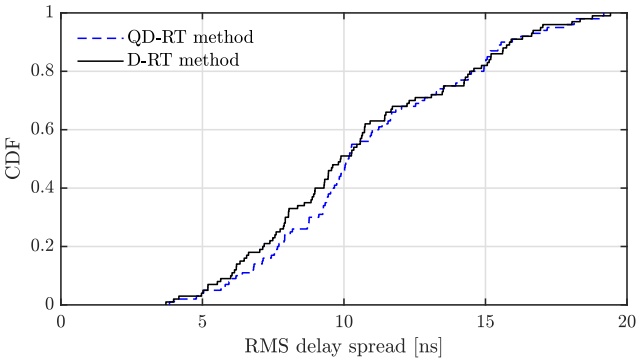

Fig. 7: RMS delay spread $\sigma_\tau[ns]$.

distributions is rigorously assessed through the Two-Sample Kolmogorov–Smirnov test (KS-test). The KS-test statistic (D_{KS}) is computed as the supremum of the absolute difference between the CDF of the random variable X_1 and the CDF of the estimated distribution X_2 as :

$$D_{\text{KS}} = \max(|F(X_1) - F(X_2)|), \tag{14}$$

where $F(X)$ denotes the CDF of X. The distributions are subjected to the KS-test at a significance level of α to rigorously confirm their quality of fit [38]. In our analysis, $\alpha = 5\%$ is considered. The obtained results consistently demonstrate a KS-test passing rate exceeding 94% for all examined distributions.

The 90$^{\text{th}}$ percentile values for the RMS delay and azimuth spread are 19 ns and 1.8 degrees, respectively. The azimuth spread indicates that the majority of the signal propagates along a specific direction rather than scattering in multiple directions. Additionally, considering the received power, the 90$^{\text{th}}$ percentile path loss is measured at 87 dB.

C. Computational time analysis

Note that the only difference between ray tracing methods and our method is the technique used to determine the bistatic RCS of irregular objects. This is typically the only part where no closed-form formulas are available and where a computationally intensive numerical solution is necessary. The

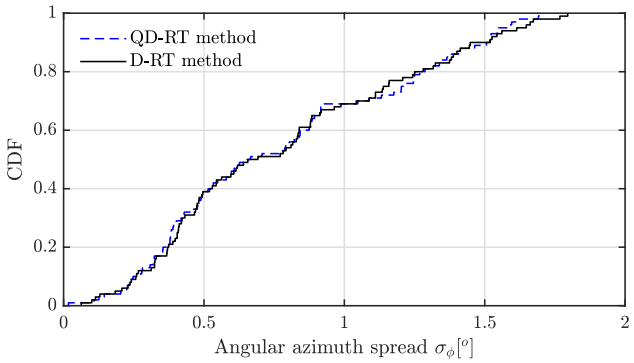

Fig. 8: RMS azimuth angular spread $\sigma_\phi[^o]$.

TABLE III: Total run time for a single incident/scattered angle from an irregular object.

Software	EM-Solver	Number of facets	Times [s]
Altair-FEKO	RL-GO*	6346	83
In-house reference	PO-Gordon	6346	4
QD-RT	Statistical RCS	NA	0.04

*Ray Launching Geometrical Optics.

bistatic RCS of a pedestrian with the dimensions listed in Table I is computed at 60 GHz for a single incident/reflection angle using PO-Gordon, QD-RT (based on the PDF of the bistatic RCS), and the ray tracing method used in commercial software. Computation times are assessed in Table III by comparing with well-known commercial solvers, i.e. Altair FEKO, and with an in-house developed PO-Gordon-based method. In this study, a total of 20 samples over elevation angle and 360 samples for azimuth angles are used. The assessment involved examining the computation times for a single incident elevation/azimuth angle and performing matrix computations for 20 scattered elevation angles and 360 scattered azimuth angles. Combining 20 samples over the elevation angle and 360 samples over the azimuth angle, our methodology generated a remarkable 7200 spatial angular points for each irregular object. The computation process involved parallel computation techniques that employed matrix computations over scattered points. It should be noted that this

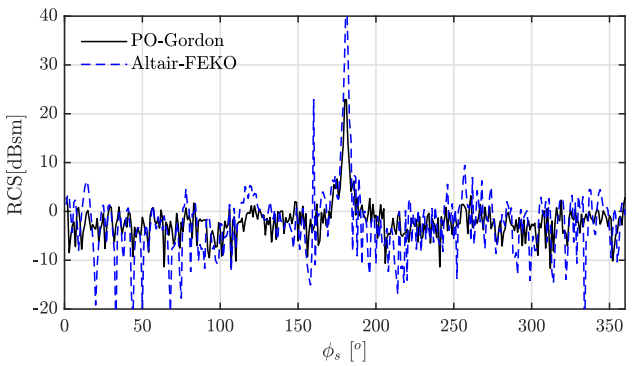

Fig. 9: Comparison of bistatic RCS of a pedestrian at 60 GHz.

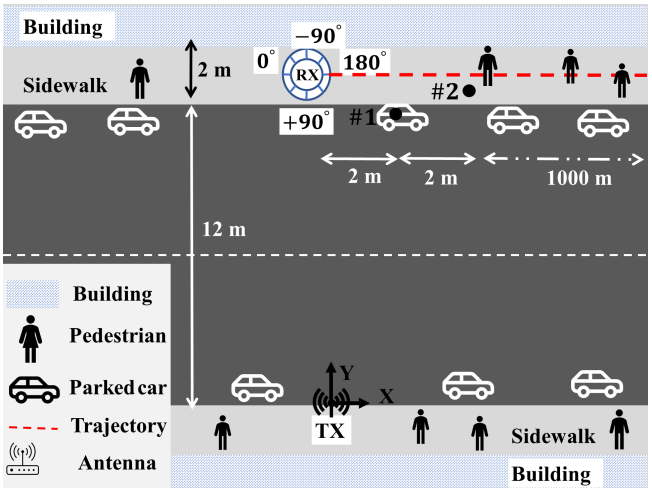

Fig. 10: Street canyon scenario including walls, parked cars, and pedestrians.

computation is computationally intensive and requires 8 hours to complete.

All simulations are done on a personal laptop with a core i7 processor, 1.70 GHz clock frequency, and 16 GB RAM. The QD-RT outperforms all other methods by far. It benefits from a low computational time thanks to the statistical model used to determine the RCS. Also, the PO-Gordon method is faster compared with Altair FEKO.

The accuracy of the proposed PO-Gordon method is examined in Fig. 9 by comparing the bistatic RCS of the pedestrian over all the scattered azimuth angles for an incident elevation/azimuth angle of 90/0 degrees and a scattered elevation angle of 90 degrees.

IV. Application of QD-RT for 3GPP Channel Modeling

This section shows that QD-RT can be helpful for developing 3GPP-like statistical channel modeling for a street canyon scenario that includes walls, pedestrians, and parked cars, as shown in Fig. 10. The close-in path loss model for NLOS paths is provided, and a procedure similar to the 3GPP-stochastic channel model is proposed for generating the channel parameters. Finally, the statistical channel model is verified and compared with the quasi-deterministic ray tracing model.

In assessing the performance of the proposed QD-RT techniques, the Power Delay Profile (PDP) emerges as a pivotal metric. Our investigation focused on generating the PDP within a street canyon scenario depicted in Fig. 10. This involved employing both QD-RT and D-RT methods, with consideration given to the presence of 10 pedestrians and 10 parked cars randomly dispersed throughout the scenario. The receiver (RX) traces a 150-meter trajectory path, allowing for a comprehensive analysis of the channel characteristics. The resulting PDP in the delay domain is shown in Fig. 11, which reveals a combination of Line-of-Sight (LOS) signals and scattering from irregular objects. To provide a more

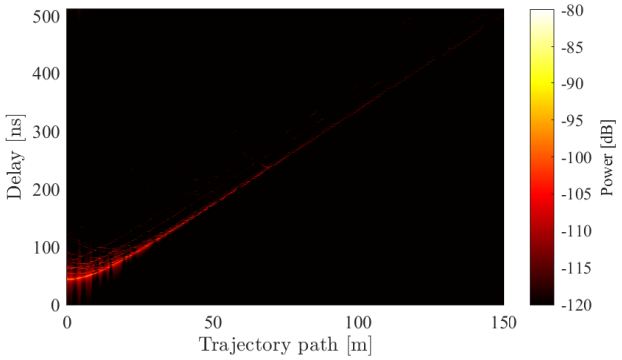

Fig. 11: Power delay profile using QD-RT method.

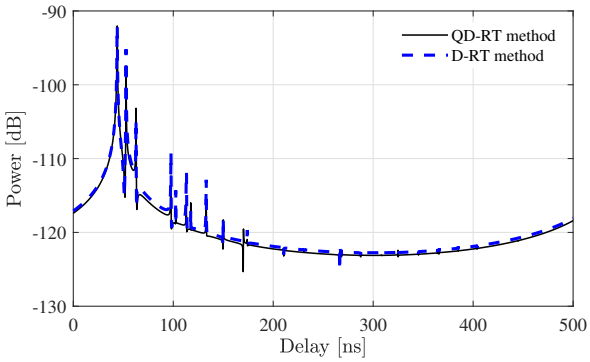

Fig. 12: Comparision of power delay profile generated with QD-RT method and D-RT method in the single snapshot position at the start point of trajectory path.

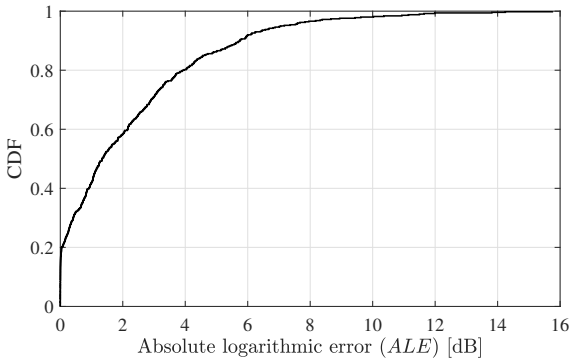

Fig. 13: CDF of the absolute logarithmic error.

detailed comparison between the QD-RT and D-RT methods, we plotted the PDP at a single snapshot position—specifically, at the beginning of the trajectory path as shown in Fig. 12. We compute the absolute logarithmic error (ALE) for the channel gain as :

$$ALE = |\bar{P}_{dB} - \hat{P}_{dB}| \tag{15}$$

where the values $\bar{P}_{dB}$ and $\hat{P}_{dB}$ represent the deterministic ray-traced channel impulse response (CIR) and the quasi-deterministic ray-traced CIRs in decibel, respectively [39]. For the PDP of Fig. 11, the ALE is computed, and it is observed that the 90$^{\text{th}}$ percentile value for the ALE error is 5.7 dB which

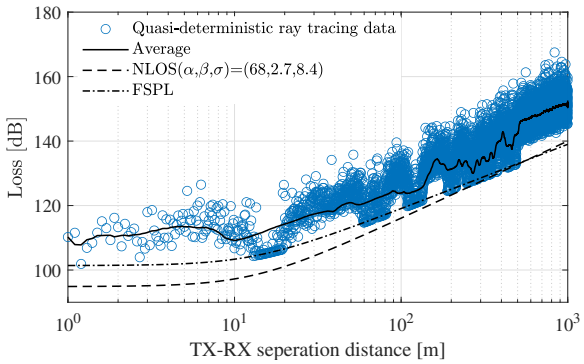

Fig. 14: Example comparison of free-space and CI path loss models separation at 60 GHz for the street canyon scenario.

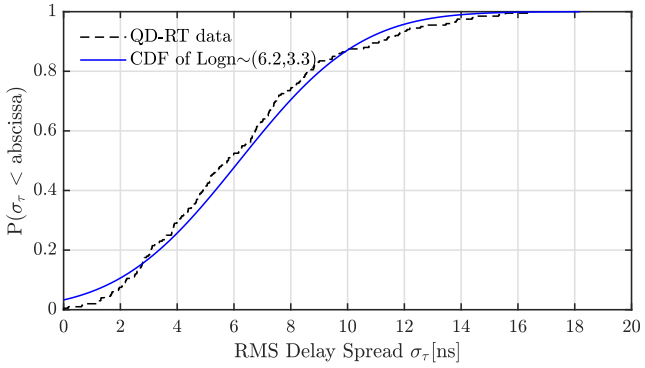

Fig. 15: RMS delay spread fitted with lognormal distribution.

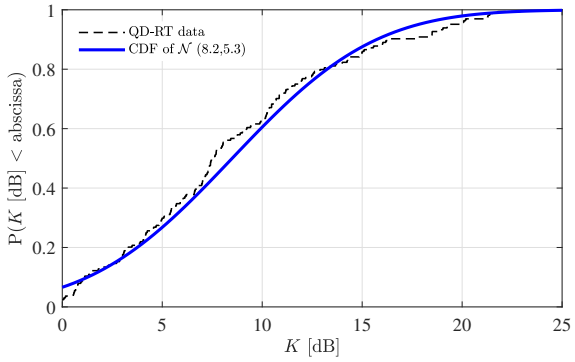

Fig. 16: K-factor parameter fitted with normal distribution.

is shown in Fig. 13. Upon closer examination, it becomes evident that the QD-RT method effectively reproduces the PDP with consistent delays, demonstrating good agreement in power levels between the two methods.

The Close-In (CI) path loss model of NLOS paths for the street canyon scenario, including irregular objects, is denoted as [40]:

$$PL^{\text{CI}} = \alpha + 10\gamma \log_{10}\left(\frac{d}{d_0}\right) + \chi_\sigma^{\text{CI}}, \quad \text{where } d > d_0, \tag{16}$$

where d_0 is the close-in free-space reference distance in meter, α denotes the intercept, f represents the operational frequency, γ represents the path loss exponent (PLE), and χ_σ^{CI} is the zero-mean Gaussian random variable with a standard deviation σ in decibels. Using the proposed path loss model based on RCS in (12), it is observed that the close-in path loss parameters for the reference distance of $d_0 = 1$ m are $\gamma = 2.7$ and $\sigma = 8.4$, respectively. Fig. 14 illustrates the NLOS path loss resulting from irregular objects. The plot incorporates the free space path loss (FSPL) attributable to LOS rays, the path loss fitted with the close-in path loss model, and the averaged NLOS path loss achieved by eliminating small-scale fading using a window size of 20 wavelengths [41].

The RMS delay spread and the K-factor are calculated using the QD-RT method [42]. These parameters are fitted with lognormal and normal distributions that are shown in Fig. 15 and Fig. 16.

The proposed close-in path loss model, the delay spread, K-factor shown in Fig. 15 and 16 can be directly implemented in a 3GPP-like approach as described in [43] using the following steps.

Step 1: Define the detailed topology, as for example in Table I.
Step 2: Calculate the LOS component as (3).
Step 3: The delay time τ_0 is calculated using (9).
Step 5: Determine the delay spread and K-factor based on the distributions given in Fig. 15 and Fig. 16.
Step 6: Determine random delays for each of the M multipath components according to Step 4 in [43], Ch. 5.3.1. Here, M and r_{DS} are set as 15 and 1.1, respectively.
Step 7: Determine random average power for individual components as described in Step 5 in [43], Ch. 5.3.1. Consider the NLOS model as in (16).
Step 8: Select the scattered phase from the uniform distribution ϕ^{r},$\phi^{\text{s}} \sim U(0, 2\pi]$.
Step 9: The channel model is the superposition of all the components as in (2).

These procedures are employed to create composite channel characteristics for the street canyon scenario. The simulation incorporates specified parameter values, and the resulting channel statistics are contrasted in Table IV. After conducting 1000 snapshots, it is observed that the assumed parameters align well with the calculated values. This showcases the efficacy of the established models and the proposed steps for model implementation. On the other hand, it is always good to use QD-RT itself since its complexity is low and coherently considers spatial consistency.

TABLE IV: Validation of statistical channel model.

Channel model	RMS delay spread [ns]	Path loss [dB]
Statistical	Logn $\sim(\mu = 1.8, \sigma = 0.45)$	Normal $\sim (\mu = 119.02, \sigma = 8.03)$
Quasi-Deterministic	Logn $\sim(\mu = 1.12, \sigma = 0.3)$	Normal $\sim (\mu = 119.048, \sigma = 8.32)$

A. *Limitations and future works*

The QD-RT method, appreciated for statistical channel analysis, faces limitations in applications demanding precise deterministic channel impulse responses like sensing. Additionally, the bistatic RCS PDF model compresses the 5D bistatic RCS (incorporating spatial angles and spatial

frequency) into a 1D function. Moreover, the study's confined focus on a pre-defined street canyon scenario with fixed dimensions and vertical polarization restricts the universality of its statistical channel model. Future efforts should involve extensive measurement experiments to validate and enhance QD-RT, enabling its harmonious amalgamation of statistical and deterministic approaches. Furthermore, exploring diverse scenarios and considering polarization effects beyond vertical-vertical (V-V) orientation are pivotal for unraveling the intricate intricacies of wireless propagation in complex settings.

V. CONCLUSIONS

A quasi-deterministic propagation model for electromagnetic waves in street canyon environments has been developed, utilizing a statistical bistatic PDF model of the RCS. It is shown that the real and imaginary parts of the bistatic scattered fields from irregular objects at mmWave follow normal distributions, and their corresponding amplitudes follow a Rayleigh distribution. The performance of the proposed quasi-deterministic model has been verified by comparing it with the D-RT method through channel characterization. The results demonstrate that both methods yield consistent distributions for second-order statistics, such as RMS delay spread and angular spread, and first-order statistics, such as the transfer function. The fact that 90$^{\text{th}}$ percentile values of RMS delay spread and path loss can be easily determined with the new model allows us to gain valuable insight into practical street canyon scenarios.

APPENDIX A. PO-GORDON FORMULATION

The scattered field from irregular objects, namely pedestrians and cars is calculated using the PO-Gordon method. The irregular objects are discretized into meshes. The scattered field from an impedance triangular mesh illuminated by a $\hat{q}$- polarized plane wave along $\hat{p}$- direction is given by

$$\vec{E}_s \cdot \hat{p} = -\frac{jk_0 Z_0 e^{jk_0 r}}{4\pi r}\alpha \iint_{S_{Lit}} e^{jk_0(\hat{k}_i - \hat{k}_s)\cdot\vec{r}} d\vec{S}, \tag{A.1}$$

where α is

$$\alpha = \{\hat{k}_{\text{s}} \times \left[\left[\hat{k}_{\text{s}} - Z_{\text{s}}/Z_0\hat{n}\right] \times Z_0\vec{J}_{\text{PO}}\right]\} \cdot \hat{p}, \tag{A.2}$$

and Z_0, k_0 are the impedance and wavenumber of free space, Z_{s} is the surface impedance of irregular object due to its conductivity [44], $\vec{r}$ is the observation point distance, $\vec{r}$ is the spherical position of integrand current and $\hat{k_s}$ is the scattered unit vector toward the observation point and $\hat{k_i}$ is the incident unit vector. It is observed that the (A.2) is frequency-independent and the frequency dependency is as:

$$E_0(\omega) = k_0 e^{jk_0 r} \iint_{S_{Lit}} e^{jk_0(\hat{k}_i - \hat{k}_s)\cdot\vec{r}} d\vec{S}. \tag{A.3}$$

It has been observed that there is a frequency dependency characterized by high fluctuations when the frequency undergoes changes. The The integral is taken over the illuminated surface S_{lit} with normal unit vector $\hat{n}$ The impressed PO current is denoted as:

$$\begin{aligned} Z_0 \cdot \vec{J}_{\text{PO}}(\vec{r}) = &\left(\hat{n} \times \hat{h}\right)(1 + R_{\text{v}})\,(\hat{q} \cdot \hat{v}) - \\ &(\hat{n} \times \hat{v})\,(1 - R_{\text{h}})\left(\hat{q} \cdot \hat{h}\right), \end{aligned} \tag{A.4}$$

which R_{v} and R_{h} are vertical and horizontal reflection coefficients denoted as

$$R_h = \frac{Z_{\text{s}}\chi - Z_0}{Z_{\text{s}}\chi + Z_0}, \tag{A.5}$$

and

$$R_v = \frac{Z_0\chi - Z_s}{Z_0\chi + Z_{\text{s}}}, \tag{A.6}$$

where $\chi = -\hat{k}_i.\hat{n}$ is the illumination coefficient that shows if the facet with normal vector $\hat{n}$ is illuminated with the incident wave.The vertical and horizontal unit vectors are $\hat{h} = \hat{k}_i \times \hat{n}$ and $\hat{v} = \hat{h} \times \hat{k}_{\text{i}}$, respectively.

The surface integral $I(\hat{k}_{\text{i}} - \hat{k}_{\text{s}}) = \iint_{S_{Lit}} e^{jk_0(\hat{k}_i - \hat{k}_s)\cdot\vec{r}} d\vec{S}$ over each mesh should be calculated. Gordon [45] showed that the double integral can be reduced to line integral using Stokes' theory as:

$$\begin{aligned} I(\vec{\zeta}) = &\frac{1}{k_0 \mid \vec{\zeta} - \left(\vec{\zeta}\cdot\hat{n}\right)\hat{n} \mid^2}\{ \\ &\sum_{m=1}^{3}\left(\vec{\zeta}\times\hat{n}\right)\cdot\Delta\vec{a}_m e^{jk_0\vec{\zeta}\cdot(\frac{\vec{a}_m+\vec{a}_{m+1}}{2})}\text{sinc}(\frac{k_0\vec{\zeta}\cdot\Delta\vec{a}_m}{2})\}, \end{aligned} \tag{A.7}$$

where $\vec{\zeta} = (\hat{k}_i - \hat{k}_s)$, $\Delta\vec{a}_m = \vec{a}_{m+1} - \vec{a}_m$, $\vec{a}_4 = \vec{a}_1$ and $\text{sinc}(x)$ represents the sinc function.

Note: Only in Appendix A, the symbols (.) and $(\times)$, represent the dot and cross products, respectively.

REFERENCES

[1] X. Cai *et al.*, "Toward 6G with terahertz communications: Understanding the propagation channels," *IEEE Communications Magazine*, 2023, to appear. [Online]. Available: https://arxiv.org/abs/2209.07864

[2] K. Du, O. Mujumdar, O. Ozdemir, E. Ozturk, I. Guvenc, M. L. Sichitiu, H. Dai, and A. Bhuyan, "60 GHz outdoor propagation measurements and analysis using facebook terragraph radios," in *2022 IEEE Radio and Wireless Symposium (RWS)*, 2022, pp. 156–159.

[3] M. Heino, J. Salmelin, and P. Wainio, "LuxTurrim5G—building the digital backbone for a smart city," *White Paper*, 2020.

[4] R. Naderpour, J. Vehmas, S. Nguyen, J. Järveläinen, and K. Haneda, "Spatio-temporal channel sounding in a street canyon at 15, 28 and 60 GHz," in *2016 IEEE 27th Annual International Symposium on Personal, Indoor, and Mobile Radio Communications (PIMRC)*, 2016, pp. 1–6.

[5] C. Oestges, G. Hennaux, and Q. Gueuning, "Centimeter- and millimeter-wave channel modeling using ray-tracing for 5G communications," in *2015 IEEE 82nd Vehicular Technology Conference (VTC2015-Fall)*, 2015, pp. 1–5.

[6] T. S. Rappaport, Y. Xing, G. R. MacCartney, A. F. Molisch, E. Mellios, and J. Zhang, "Overview of millimeter wave communications for fifth-generation (5G) wireless networks—with a focus on propagation models," *IEEE Transactions on Antennas and Propagation*, vol. 65, no. 12, pp. 6213–6230, 2017.

[7] M. Rybakowski and J.-M. Conrat, "White Paper W2.1 6–100 GHz Channel Modelling for 5G: Measurement and Modelling Plans in mmMAGIC," 2016.

[8] D. Dupleich, R. Müller, M. Landmann, E.-A. Shinwasusin, K. Saito, J.-I. Takada, J. Luo, R. Thomä, and G. Del Galdo, "Multi-band propagation and radio channel characterization in street canyon scenarios for 5G and beyond," *IEEE Access*, vol. 7, pp. 160 385–160 396, 2019.

[9] L. Ahumada, E. Carreño, A. Anglès, and D. Schkolnik, "Shadowing correlation: Empirical results for mm-wave wireless links in urban street canyons," *IEEE Antennas and Wireless Propagation Letters*, vol. 17, no. 4, pp. 543–546, 2018.

[10] T. S. Rappaport, G. R. MacCartney, M. K. Samimi, and S. Sun, "Wideband millimeter-wave propagation measurements and channel models for future wireless communication system design," *IEEE Transactions on Communications*, vol. 63, no. 9, pp. 3029–3056, 2015.

[11] R. J. Weiler, M. Peter, W. Keusgen, A. Maltsev, I. Karls, A. Pudeyev, I. Bolotin, I. Siaud, and A.-M. Ulmer-Moll, "Quasi-deterministic millimeter-wave channel models in MiWEBA," *EURASIP Journal on Wireless Communications and Networking*, vol. 2016, no. 1, pp. 1–16, 2016.

[12] C. Lai, R. Sun, C. Gentile, P. B. Papazian, J. Wang, and J. Senic, "Methodology for multipath-component tracking in millimeter-wave channel modeling," *IEEE Transactions on Antennas and Propagation*, vol. 67, no. 3, pp. 1826–1836, 2019.

[13] H. Assasa, J. Widmer, T. Ropitault, and N. Golmie, "Enhancing the NS-3 IEEE 802.11 ad model fidelity: Beam codebooks, multi-antenna beamforming training, and quasi-deterministic millimeter-wave channel," in *Proceedings of the 2019 Workshop on ns-3*, 2019, pp. 33–40.

[14] M. Lecci, M. Polese, C. Lai, J. Wang, C. Gentile, N. Golmie, and M. Zorzi, "Quasi-deterministic channel model for millimeter-wave: Mathematical formalization and validation," in *GLOBECOM 2020 - 2020 IEEE Global Communications Conference*, 2020, pp. 1–6.

[15] N. Varshney, J. Wang, C. Lai, C. Gentile, R. Charbonnier, and Y. Corre, "Quasi-deterministic channel propagation model for an urban environment at 28 GHz," *IEEE Antennas and Wireless Propagation Letters*, vol. 20, no. 7, pp. 1145–1149, 2021.

[16] S. Dorokhin, P. Lysov, A. Aderkina, and V. Lyashev, "Reconfigurable intelligent surface MIMO simulation using quasi deterministic radio channel model," *arXiv preprint arXiv:2211.12601*, 2022.

[17] S. Y. Jun, C. Lai, D. Caudill, J. Wang, J. Senic, N. Varshney, and C. Gentile, "Quasi-deterministic channel propagation model for 60 GHz urban Wi-Fi access from light poles," *IEEE Antennas and Wireless Propagation Letters*, vol. 21, no. 8, pp. 1517–1521, 2022.

[18] K. Guan, Z. Zhong, M. L. Nicolás, R. Geise, B. Neubauer, G. Zimmer, and T. Kürner, "Measurement and simulation of the bistatic radar cross section of traffic signs for vehicle-to-x communications," in *7th European Conference on Antennas and Propagation (EuCAP)*. IEEE, 2013, pp. 2565–2569.

[19] K. Guan, B. Ai, M. L. Nicolas, R. Geise, A. Möller, Z. Zhong, and T. Kürner, "On the influence of scattering from traffic signs in vehicle-to-x communications," *IEEE Transactions on Vehicular Technology*, vol. 65, no. 8, pp. 5835–5849, 2015.

[20] G. Gougeon, Y. Lostanlen, and L. Maviel, "Coupling a deterministic propagation model with diffuse scattering and urban furniture for small cells," in *Proceedings of the 5th European Conference on Antennas and Propagation (EUCAP)*. IEEE, 2011, pp. 3448–3452.

[21] V. Nurmela, A. Karttunen, A. Roivainen, L. Raschkowski, V. Hovinen, J. Y. EB, N. Omaki, K. Kusume, A. Hekkala, R. Weiler *et al.*, "Deliverable D1.4 METIS channel models," *Proc. Mobile Wireless Commun. Enablers Inf. Soc.(METIS)*, p. 1, 2015.

[22] A. Lahuerta-Lavieja, M. Johansson, C. Larsson, U. Gustavsson, and G. A. Vandenbosch, "Computationally efficient millimeter-wave scattering models: A multiple-scattering model," *IEEE Transactions on Antennas and Propagation*, vol. 70, no. 9, pp. 8250–8261, 2022.

[23] ——, "Computationally efficient millimeter-wave scattering models: A combined blockage and backscattering model," *IEEE Antennas and Wireless Propagation Letters*, vol. 21, no. 9, pp. 1852–1856, 2022.

[24] A. L. Lavieja, "Computationally efficient mm-wave scattering models," 2021.

[25] G. Li, B. Ai, G. L. Stüber, K. Guan, and G. Shi, "On the modeling of near-field scattering of vehicles in vehicle-to-x wireless channels based on scattering centers," *IEEE Access*, vol. 7, pp. 3264–3274, 2018.

[26] M. I. Skolnik, "Introduction to radar," *Radar handbook*, vol. 2, p. 21, 1962.

[27] J. Ebrahimizadeh, E. Vinogradov, and G. A. Vandenbosch, "RCS-based quasi-deterministic ray tracing for statistical channel modeling," *arXiv preprint arXiv:2307.04498*, 2023.

[28] J. Ebrahimizadeh, V. Khorashadizadeh, X. Cai, and G. A. Vandenbosch, "Polarimetric bistatic RCS distribution: A sensing metric for 5G wireless," *Communication" 2023 IEEE Globecom Workshops (GC Wkshps)*, 2023.

[29] S. J. Myint, C. Schneider, M. Röding, G. Del Galdo, and R. S. Thomä, "Statistical analysis and modeling of vehicular radar cross section," in *13th European Conference on Antennas and Propagation (EuCAP)*. IEEE, 2019, pp. 1–5.

[30] 3D model renderhub. "(. [Online]. Available: https://www.renderhub.com/wirecase3d/3d-city-rt-day

[31] Y. Pinhasi, A. Yahalom, and S. Petnev, "Propagation of ultra wide-band signals in lossy dispersive media," in *IEEE International Conference on Microwaves, Communications, Antennas and Electronic Systems*. IEEE, 2008, pp. 1–10.

[32] R. ITU, "Electrical characteristics of the surface of the earth," *ITU-R P. 527-4*, 2017.

[33] W. C. Chew, *Waves and fields in inhomogenous media*. John Wiley & Sons, 1999, vol. 16.

[34] K. Sato, H. Kozima, H. Masuzawa, T. Manabe, T. Ihara, Y. Kasashima, and K. Yamaki, "Measurements of reflection characteristics and refractive indices of interior construction materials in millimeter-wave bands," in *IEEE 45th Vehicular Technology Conference. Countdown to the Wireless Twenty-First Century*, vol. 1. IEEE, 1995, pp. 449–453.

[35] X. Cai, "Autonomous vehicles: Mmw radar backscattering modeling of traffic environment, vehicular communication modeling, and antenna designs," Ph.D. dissertation, 2020.

[36] X. Cai, M. Giallorenzo, and K. Sarabandi, "Machine learning-based target classification for mmw radar in autonomous driving," *IEEE Transactions on Intelligent Vehicles*, vol. 6, no. 4, pp. 678–689, 2021.

[37] X. Cai, G. Zhang, C. Zhang, W. Fan, J. Li, and G. F. Pedersen, "Dynamic channel modeling for indoor millimeter-wave propagation channels based on measurements," *IEEE Transactions on Communications*, vol. 68, no. 9, pp. 5878–5891, 2020.

[38] R. He, Z. Zhong, B. Ai, and C. Oestges, "Shadow fading correlation in high-speed railway environments," *IEEE Transactions on Vehicular Technology*, vol. 64, no. 7, pp. 2762–2772, 2014.

[39] J. Hoydis, F. A. Aoudia, S. Cammerer, F. Euchner, M. Nimier-David, S. t. Brink, and A. Keller, "Learning radio environments by differentiable ray tracing," *arXiv preprint arXiv:2311.18558*, 2023.

[40] S. Sun, T. S. Rappaport, T. A. Thomas, A. Ghosh, H. C. Nguyen, I. Z. Kovacs, I. Rodriguez, O. Koymen, and A. Partyka, "Investigation of prediction accuracy, sensitivity, and parameter stability of large-scale propagation path loss models for 5G wireless communications," *IEEE transactions on vehicular technology*, vol. 65, no. 5, pp. 2843–2860, 2016.

[41] X. Cai, A. Gonzalez-Plaza, D. Alonso, L. Zhang, C. B. Rodríguez, A. P. Yuste, and X. Yin, "Low altitude UAV propagation channel modelling," in *2017 11th European Conference on Antennas and Propagation (EUCAP)*. IEEE, 2017, pp. 1443–1447.

[42] X. Cai, X. Yin, X. Cheng, and A. P. Yuste, "An empirical random-cluster model for subway channels based on passive measurements in UMTS," *IEEE Transactions on Communications*, vol. 64, no. 8, pp. 3563–3575, 2016.

[43] Technical Specification Group Radio Access Network;, "Spatial Channel Model for Multiple Input Multiple Output (MIMO) Simulations," 3rd Generation Partnership Project, Tech. Rep. 3GPP TR 25.996 V13.0.0, 2015, 3rd Generation Partnership Project, Document.

[44] K. M. Mitzner, "An integral equation approach to scattering from a body of finite conductivity," *Radio Science*, vol. 2, no. 12, pp. 1459–1470, 1967.

[45] W. Gordon, "Far-field approximations to the kirchoff-helmholtz representations of scattered fields," *IEEE Transactions on Antennas and Propagation*, vol. 23, no. 4, pp. 590–592, 1975.